communications materials

A Nature Portfolio journal

Article

https://doi.org/10.1038/s43246-025-00969-y

Transforming pomelo peel waste into multifunctional biomaterials for hemostasis and wound healing

Wenbing Wan[1], Jianqiu Yang[1,2], Zhenzhen Huang[2], Yang Feng[2], Zhengquan Wang[3] ✉ & Shixuan Chen[2] ✉

Pomelo peel (PP), an abundant yet underutilized by-product of fruit consumption, holds immense potential for biomedical innovation due to its porous structure and bioactive compounds. Here we show an eco-friendly transformation of PP into high-performance materials for hemostasis and wound care using scalable manufacturing methods: CO_2 expansion and carbonization. The resulting expanded decellularized pomelo peel (EDPP) sponges exhibit rapid liquid absorption, exceptional porosity, and shape recovery, enabling efficient platelet activation and accelerated hemostasis. In a diabetic wound healing model, EDPP significantly outperformed commercial dressings by enhancing granulation tissue formation, collagen deposition, and wound closure. The carbonized pomelo peel (CPP) aerogels leverage photothermal effects to eradicate bacterial biofilms, promoting the healing of infected wounds. These sustainable materials, derived from agricultural waste, provide innovative solutions for critical healthcare challenges, reducing environmental waste while addressing the global demand for effective wound management systems.

Nature is a vast treasure trove, offering not only abundant food, fruits, and vegetables for human sustenance but also herbal medicines for treating various diseases. Biomedical devices derived from natural plants leverage the therapeutic properties of inherent structures and compounds of plants for various biomedical applications, ranging from wound healing and tissue regeneration to disease diagnostics and treatment[1]. For instance, the hierarchical structures and unique topography patterns make them invaluable for regenerative medicine applications[2,3]. These structures and topographies contribute to cellular migration, growth, and differentiation, facilitating tissue repair and regeneration in damaged organs. Additionally, the main components of plants, such as cellulose, lignin, or chitosan, have been widely utilized in wound dressings, scaffolds, and drug delivery systems due to their biocompatibility and biodegradability[4]. Moreover, bioactive compounds derived from plants, such as flavonoids, polyphenols, alkaloids, and terpenoids, have been incorporated into modern medical practices[5]. These plant-derived drugs are used to treat a variety of conditions, including pain, inflammation, and infections. Therefore, biomedical devices inspired by natural plants hold great promise in addressing diverse medical challenges.

The pomelo is one of the most consumed fruits. Pomelo peel (PP), a by-product of pomelo consumption, is beneficial due to its porous internal structure and richness in various functional compounds (e.g., essential oil, pectin, and polyphenols)[6,7]. However, much of this by-product is currently wasted. Utilizing pomelo peels could not only result in value-added products and ingredients but also mitigate environmental threats. The processing of biomaterial scaffolds is inseparable from advanced processing technology. From the perspective of realizing the commercialization of developed biomedical devices, the manufacturing technology should not be too complicated, and it should not produce a large amount of wastewater and other pollutants during the manufacturing process. In our previous work, we reported a simple approach for preparing 3D nanofiber scaffolds via depressurization of subcritical CO_2 fluid[8]. This method addresses many issues associated with traditional techniques, such as the need for aqueous solutions, chemical reactions, and the loss of activity of encapsulated biological molecules. It is non-toxic, inexpensive, and environmentally friendly, making it suitable for expanding PP to increase its porosity and extend its applications in the biomedical field. Additionally, since the main component of PP is cellulose, it can be carbonized through a hydrothermal reaction to produce carbon-based materials with photothermal effects, which can be used for wound dressings[9,10]. This process holds promise for creating safe and effective photothermal antibacterial dressings.

[1]Department of Orthopaedic Surgery, Institute of Orthopedics of Jiangxi Province, Jiangxi Provincial Key Laboratory of Spine and Spinal Cord Disease, The Second Affiliated Hospital of Nanchang University, Nanchang, Jiangxi, China. [2]Zhejiang Engineering Research Center for Tissue Repair Materials, Wenzhou Institute, University of the Chinese Academy of Sciences, Wenzhou, Zhejiang, China. [3]Department of Emergency Medicine, The Affiliated Yangming Hospital of Ningbo University, Ningbo, Zhejiang, China. ✉e-mail: 13777106152@163.com; chensx@ucas.ac.cn

In this study, we developed two distinct biomaterials from PP: an expanded decellularized pomelo peel (EDPP) sponge for rapid hemostasis and a carbonized pomelo peel (CPP) aerogel for photothermal-assisted wound healing (Fig. 1). EDPP demonstrated rapid liquid absorption and platelet activation, achieving superior hemostatic performance compared to commercial gelatin sponges. CPP, with its stable photothermal properties, eradicated bacterial biofilms and accelerated wound healing in infected skin. These findings highlight the versatility and efficacy of PP-derived biomaterials, offering sustainable and scalable solutions to address pressing clinical challenges in wound management and hemostasis.

Results

Preparation and characterization of the decellularized pomelo peel sponge

The outer yellow rind of the raw pomelo peel (PP) was initially removed to expose the faint yellow inner peel. The inner peel was subsequently shaped

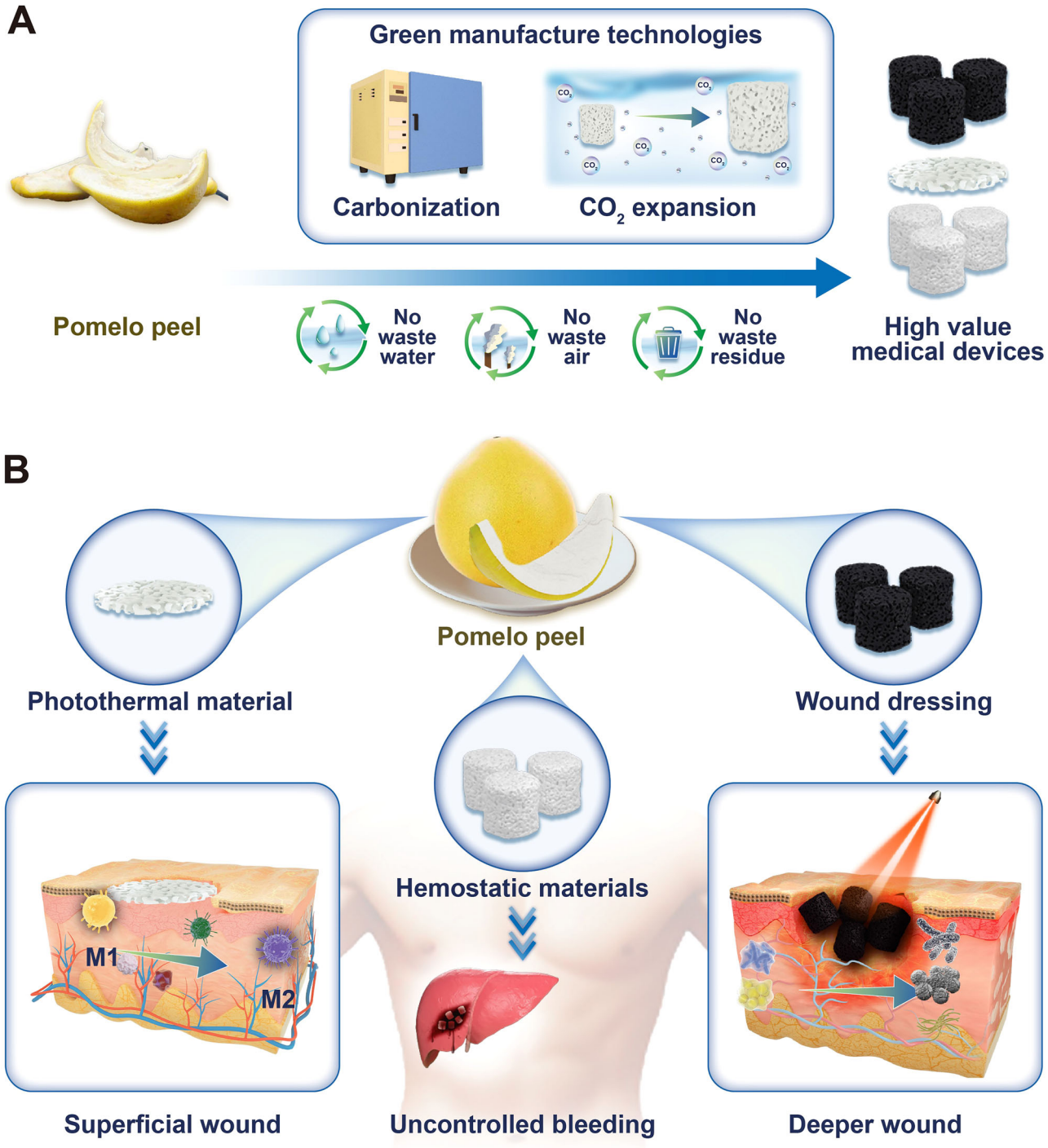

Fig. 1 | Research and development of high-value medical devices based on waste pomelo peels. A The purpose of this study is to develop pomelo peel (PP) into biomedical devices for rapid hemostasis and wound management through two green manufacturing techniques, carbonization and depressurization of subcritical CO_2 fluid. **B** For one thing, the PP was decellularized (DPP) and then expanded by depressurization of subcritical CO_2 fluid to increase its porosity. The expanded DPP (EDPP) could be used as a wound dressing and hemostatic material. For another, the PP was carbonized to create a carbon-based material with photothermal properties to effectively eradicate bacterial biofilms.

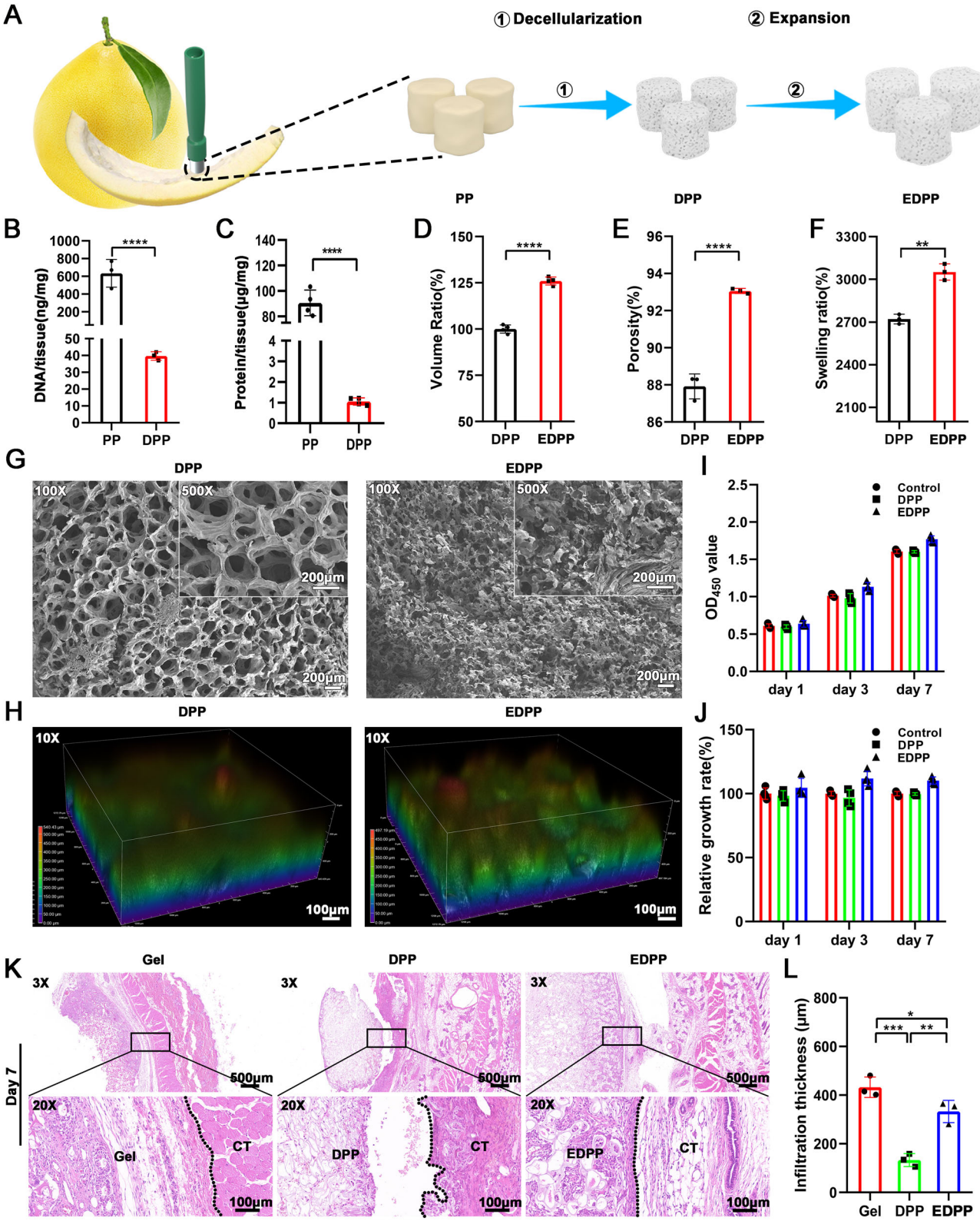

into cylindrical forms and subjected to decellularization by soaking it in sodium hypochlorite and Triton-X100, resulting in the decellularized pomelo peel (DPP) (Fig. 2A and Supplementary Fig. 1). As shown in Supplementary Fig. 1, the faint yellow pomelo peel (PP) turns white after decellularization, becoming the decellularized pomelo peel (DPP). The DNA content of the DPP sponge was 36.17 ± 2.52 ng/mg, significantly lower than that of PP (633.67 ± 157.36 ng/mg), suggesting 94.29% of DNA was removed (Fig. 2B). Similarly, the protein content of the DPP sponge was 1.05 ± 0.18 μg/mg, notably lower than that of PP at 90.57 ± 10.09 μg/mg, indicating a deproteinization degree of approximately 98.84% (Fig. 2C).

Then, the DPP was expanded via depressurization of subcritical CO_2 fluid to increase its porosity further (Fig. 2A and Supplementary Fig. 1). After expansion, the volume of the expanded DPP (EDPP) increased by 25.98% compared to that of the original DPP (Fig. 2D), and the porosity of

Fig. 2 | Preparation and characterization of the expanded decellularized pomelo peel (foam). **A** The flow chart introduces the manufacturing processes of the decellularized pomelo peel, including decellularization and CO_2 depressurization. **B** DNA content of the pomelo peel before and after decellularization. **C** Protein content of the pomelo peel before and after decellularization. **D** Volume ratio before and after decellularization. **E** The porosity of the decellularized pomelo peel before and after CO_2 depressurization. **F** The swelling ratio of the decellularized pomelo peel before and after CO_2 depressurization. **G** SEM images of the internal structure of the decellularized pomelo peel in cross-section. **H** Characterization of surface roughness of the decellularized pomelo peel and expanded DPP foam (EDPP) with confocal laser scanning microscopy. **I** Cytotoxicity assay of DPP and expanded DPP foam (EDPP) to L929 cells after co-culturing for 1, 3, and 7 days. **J** The relative growth rate (RGR, %) of L929 cells after co-culturing with the extracts of DPP and expanded DPP foam (EDPP) for 1, 3, and 7 days. **K** Histological observations of the interfaces between hemostatic materials and connective tissues. The black dashed line refers to the boundary of the injured skin tissues and the hemostatic materials. **L** Infiltration thickness and density of cell infiltration after 7 days of subcutaneous implantation by DPP, EDPP, and gelatin sponge. $^{*}p < 0.05$, $^{**}p < 0.01$, $^{***}p < 0.001$, $^{****}p < 0.0001$ (n = 3–4).

EDPP (93.06 ± 0.14%) was higher than that of DPP (87.92 ± 0.67%) (Fig. 2E), resulting in the swelling rates of EDPP ((3152 ± 57)%) was increased compared to DPP ((2718 ± 23)%) (Fig. 2F). Prior to expansion, the internal structure of the DPP exhibited a porous structure. Following expansion with subcritical CO_2 fluid, the original pore structure of the DPP was completely disrupted, transforming into a lamellar structure in the EDPP (Fig. 2G). Moreover, we also found that the surface roughness of the EDPP was significantly enhanced compared to that of DPP (Fig. 2H).

Furthermore, we also examined the cellular and tissue compatibility of EDPP. We initially examined the impact of DPP and EDPP extracts on cell proliferation. The extracts from both DPP and EDPP showed no effect on the proliferation of L929 cells (Fig. 2I). Additionally, Live/Dead staining indicated no significant presence of dead cells after 1, 3, and 7 days of co-culture (Supplementary Fig. 2). The relative growth rate (%) of DPP and EDPP was close to 100%, suggesting no cytotoxicity (Fig. 2J). In addition, we also tested the tissue compatibility of the DPP and EDPP through subcutaneous implantation. After 7 days of implantation, the degradation rate of DPP and EDPP sponges was slower than that of the positive control Gelfoam group. Additionally, the degradation rate of EDPP was faster than that of DPP. By day 28 of implantation, the Gelfoam completely degraded, while the DPP and EDPP sponges degraded by 73.62 ± 2.44% and 76.40 ± 2.24%, respectively (Supplementary Fig. 3). The histological observations further revealed that significant cell infiltration was observed at the boundary between the material and the skin in all groups (Fig. 2K). The infiltrated thickness in the EDPP group (332.7 ± 49.37) μm was significantly higher than in the DPP group (108.3 ± 6.801) μm (Fig. 2L). Additionally, there was no apparent fibrous capsule formed in the EDPP group compared to the DPP group after 7 days of subcutaneous implantation, indicating that the expansion treatment by subcritical CO_2 fluid may reduce tissue rejection of DPP. The cell infiltration and cell density were further enhanced after 14 days of implantation (Supplementary Fig. 4).

EDPP wound dressing promotes diabetic wound healing

The EDPP was processed into 1 mm thick dressings with various areas and shapes to accommodate different types of wounds (Fig. 3A). We verified the wound repair effect of EDPP in the skin wound model of type 2 diabetic mice (Fig. 3B). The commonly clinically used wound dressings, Lando and PELNAC, were utilized as positive controls. The wounds and wound healing ratio photographs indicated that the wound closure speed of the EDPP and PELNAC groups is faster than that of the other blank controls, including the DPP and Lando groups (Supplementary Fig. 5 and Fig. 3C, D).

Histological observation showed no apparent granulation tissue hyperplasia in each group 3 days after surgery (Supplementary Fig. 6). Seven days after surgery, significant granulation tissue was formed in the DPP, EDPP, Lando, and PELNAC groups (Supplementary Fig. 6). There was obvious collagen deposition and newly formed blood vessels within the new granulation tissue (Fig. 3F, G). Fourteen days after surgery, all 4 groups had completed re-epithelialization, and there was no difference in the speed of re-epithelialization between the EDPP and the PELNAC groups (Supplementary Fig. 6 and Fig. 3E). However, dense collagen fibers existed in the new dermis of the four groups (Supplementary Fig. 7). On the 21st day after surgery, the collagen in the new dermal tissue in each group had completed rearrangement (Supplementary Fig. 7).

Moreover, we examined the expression of immune cells among 4 groups after 7 days of treatment. The expression of CD45 (a pan marker of leukocytes) (Supplementary Fig. 8A, C) and Ly6G (a pan marker of neutrophils, monocytes, and granulocytes) (Supplementary Fig. 8B, D) in the PELNAC and EDPP groups was lower than the control, DPP, and Lando groups. The CD45 and Ly6G expression of the PELNAC group was significantly reduced compared to the EDPP groups. We also assessed the expression of macrophages, the primary cells involved in the inflammatory response. The expression of CCR7 (a marker of M1-type macrophage) of the control, DPP, and Lando groups was significantly higher than that of the EDPP and PELNAC groups (Fig. 3H, I). Conversely, the expression of CD206 (a marker of M2-type macrophages) in the control, DPP, and Lando groups was significantly lower than in the EDPP and PELNAC groups (Fig. 3J, K). The ratio between the numbers of M1-type and M2-type macrophages of the control, DPP, and Lando groups was greater than 1, suggesting these three groups were dominated by pro-inflammatory responses on day 7. By comparison, the EDPP and PELNAC groups were dominated by pro-regenerative responses on day 7 (Fig. 3L).

The potential pro-healing mechanism of the EDPP

RNA-seq analysis was conducted on skin wound tissue (Day 7) to elucidate the potential pro-healing mechanisms of EDPP. Principal component analysis (PCA) demonstrated that the selected skin wound tissues exhibited good consistency, allowing further in-depth analysis (Fig. 4A). The volcano plot identified 110 down-regulated genes and 335 up-regulated genes in the EDPP group compared to the PELNAC group ($P < 0.05$, fold change >2.0) (Fig. 4B). The heatmap further exhibited the top 10 up-regulated (e.g., Plac8, Hck, Reg3g) and down-regulated genes (e.g., Plce1, Agt, Kcnj8) in the EDPP group compared to the PELNAC group (Fig. 4C). GO enrichment analysis revealed that these differentially expressed genes were involved in the positive regulation of immune response, anti-inflammatory processes, and wound healing activities (Fig. 4D–F). In contrast, the classical inflammatory signaling pathway PI3K/Akt was inhibited (Fig. 4I). Additionally, gene set enrichment analysis (GSEA) indicated that EDPP treatment could enhance defense responses and innate immune responses (Fig. 4G, H), aligning with the findings from the GO enrichment analysis. Moreover, we further utilized the GlueGO plug-in in Cytoscape software to perform interaction analysis on all significantly up-regulated genes identified in this experiment (Fig. 4J). The gene interaction network diagram reveals that pathways related to inflammation regulation, including positive regulation of defense response and cytokine production, were significantly enriched. These findings are consistent with the above results. Therefore, EDPP mitigates the pro-inflammatory response by promoting M2 macrophage polarization (Fig. 4K), which could prepare a ideal wound bed for wound healing.

Rapid water absorption and shape recovery ability of the EDPP

During the aforementioned wound healing experiments, we observed that EDPP effectively absorbs wound exudate and retains its shape after compression. Thus, we further studied the mechanical and water absorption properties of EDPP. Under dry conditions, the compressive stress of EDPP (2.708 ± 0.176 MPa) and DPP (3.458 ± 0.211 MPa) was significantly higher than that of the gelatin sponge (0.207 ± 0.008 MPa) at 90% compressive strain. Similarly, under wet conditions, the compressive stress of EDPP and

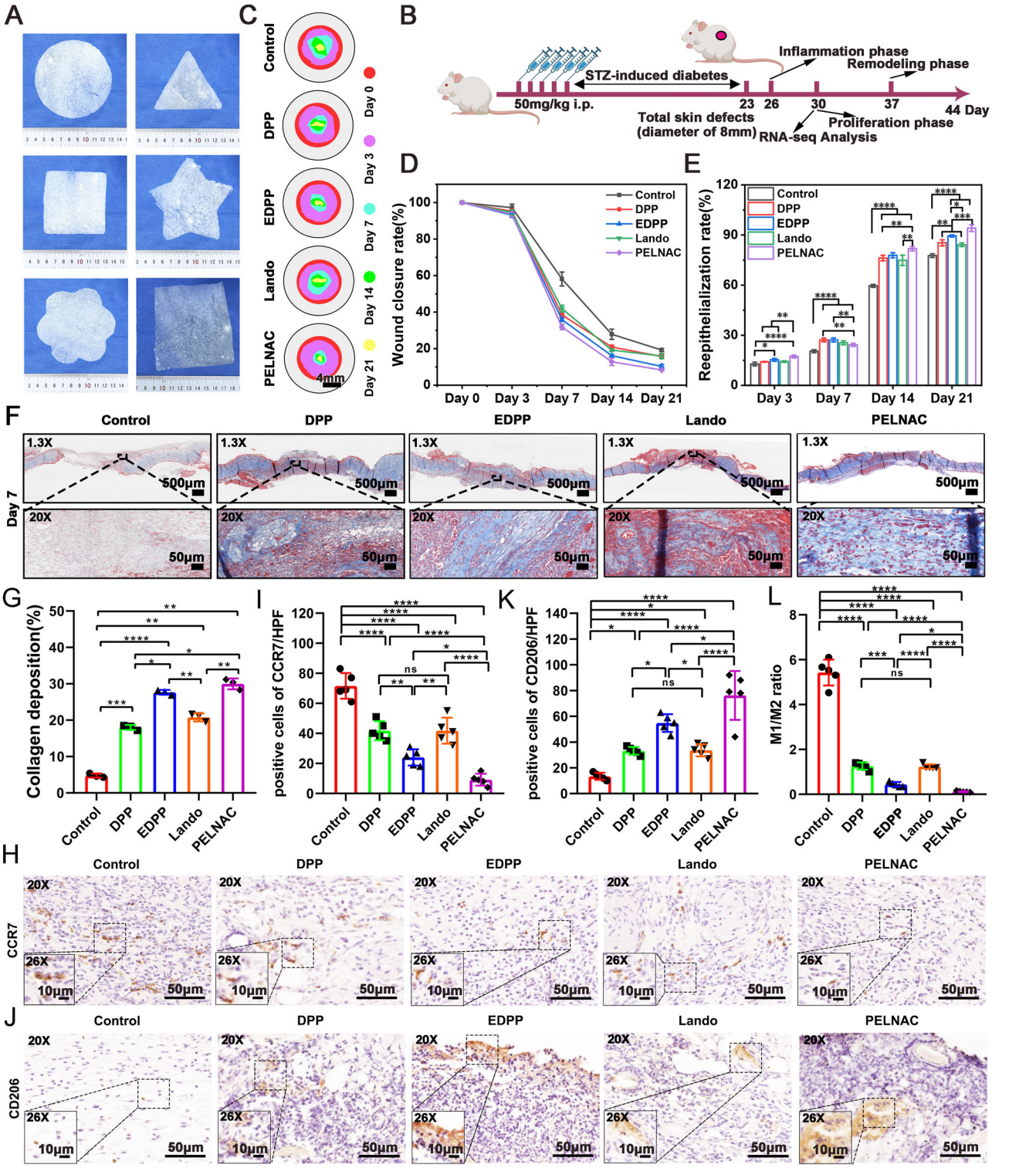

Fig. 3 | EDPP promotes diabetic wound healing. **A** The controlling of the shape and size of EDPP. **B** Timeline of the entire diabetic skin wound healing experiment, including STZ induction, wound model establishment, and RNA-seq analysis. **C**, **D** The wound closure rate of the control, DPP, EDPP, Lando, and PELNAC groups at each indicated time point. **E** The wound re-epithelialization rate of the control, DPP, EDPP, Lando, and PELNAC groups at each indicated time point. **F** The trichrome staining of the wound area in the control, DPP, EDPP, Lando, and PELNAC groups on day 7. **G** The quantification of collagen deposition at the wound area in the control, DPP, EDPP, Lando, and PELNAC groups on day 7. **H**, **I** The expression of CCR7 at the wound center area of the control, DPP, EDPP, Lando, and PELNAC groups on day 7. **J**, **K** The expression of CD206 at the wound center area of the control, DPP, EDPP, Lando, and PELNAC groups on day 7. **L** The ratio between the numbers of M1-type macrophages and the numbers of M2-type macrophages on day 7. *$p < 0.05$, **$p < 0.01$, ***$p < 0.001$, ****$p < 0.0001$ (n = 3).

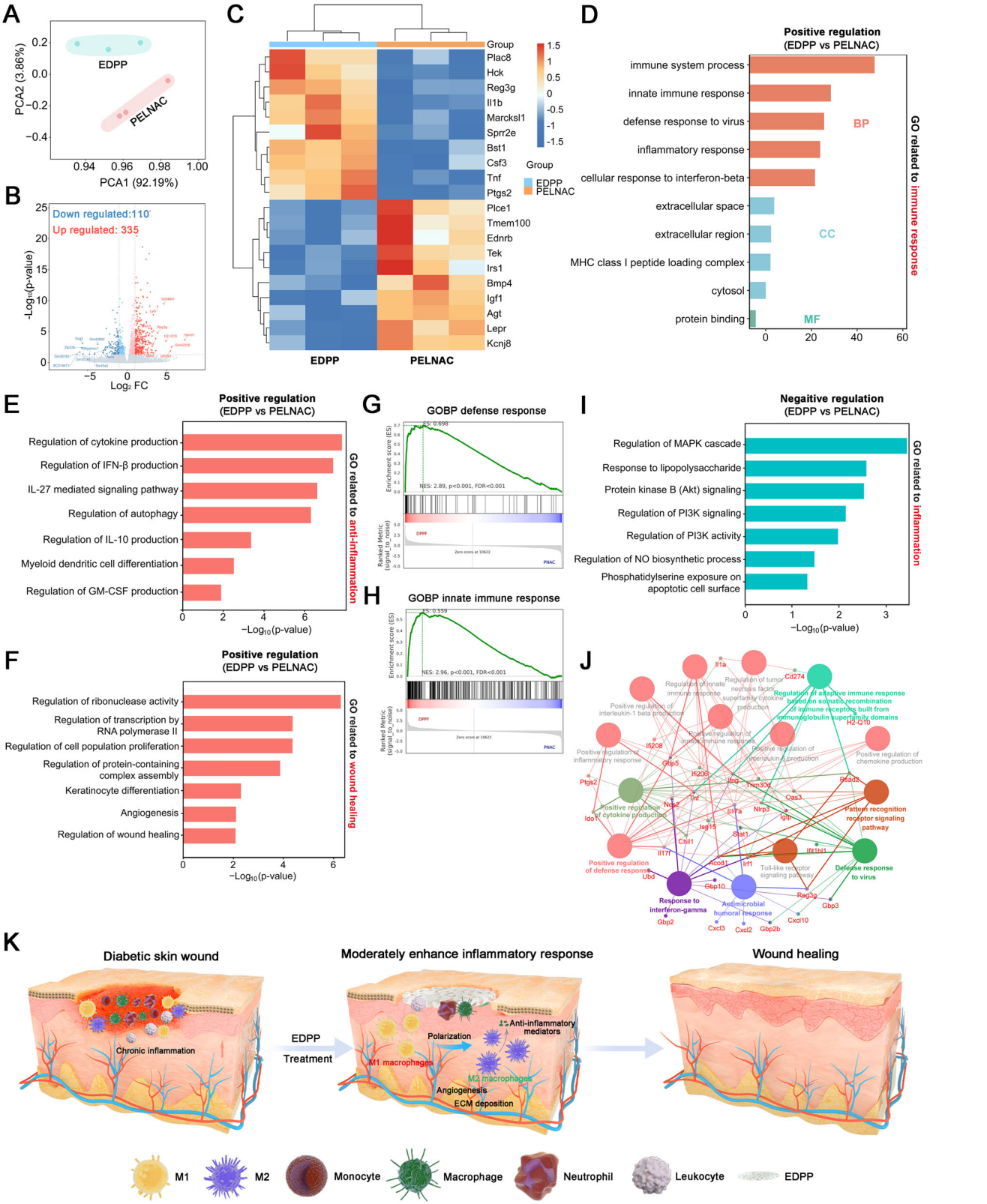

Fig. 4 | RNA-seq analysis reveals the potential pro-healing mechanism of EDPP. **A** Principal component analysis (PCA) of samples from the EDPP and PELNAC groups. **B** A volcano plot shows the up-regulated and down-regulated genes in the EDPP group compared to the PELNAC group. **C** A heatmap displaying the top 10 up-regulated and down-regulated genes in the EDPP group relative to the PELNAC group. GO enrichment analysis highlighting positive regulation of immune response (**D**), anti-inflammatory processes (**E**), and wound healing (**F**) in the EDPP group compared to the PELNAC group. **G**, **H** Representative gene set enrichment analysis (GSEA) comparing the EDPP and PELNAC groups. **I** GO enrichment analysis related to the negative regulation of inflammation in the EDPP group compared to the PELNAC group. **J** Protein-protein interaction networks of immune responses regulated by EDPP. **K** The schematic illustrates how EDPP mitigates the pro-inflammatory response by promoting M2 macrophage polarization, thereby creating a favorable wound bed for repair.

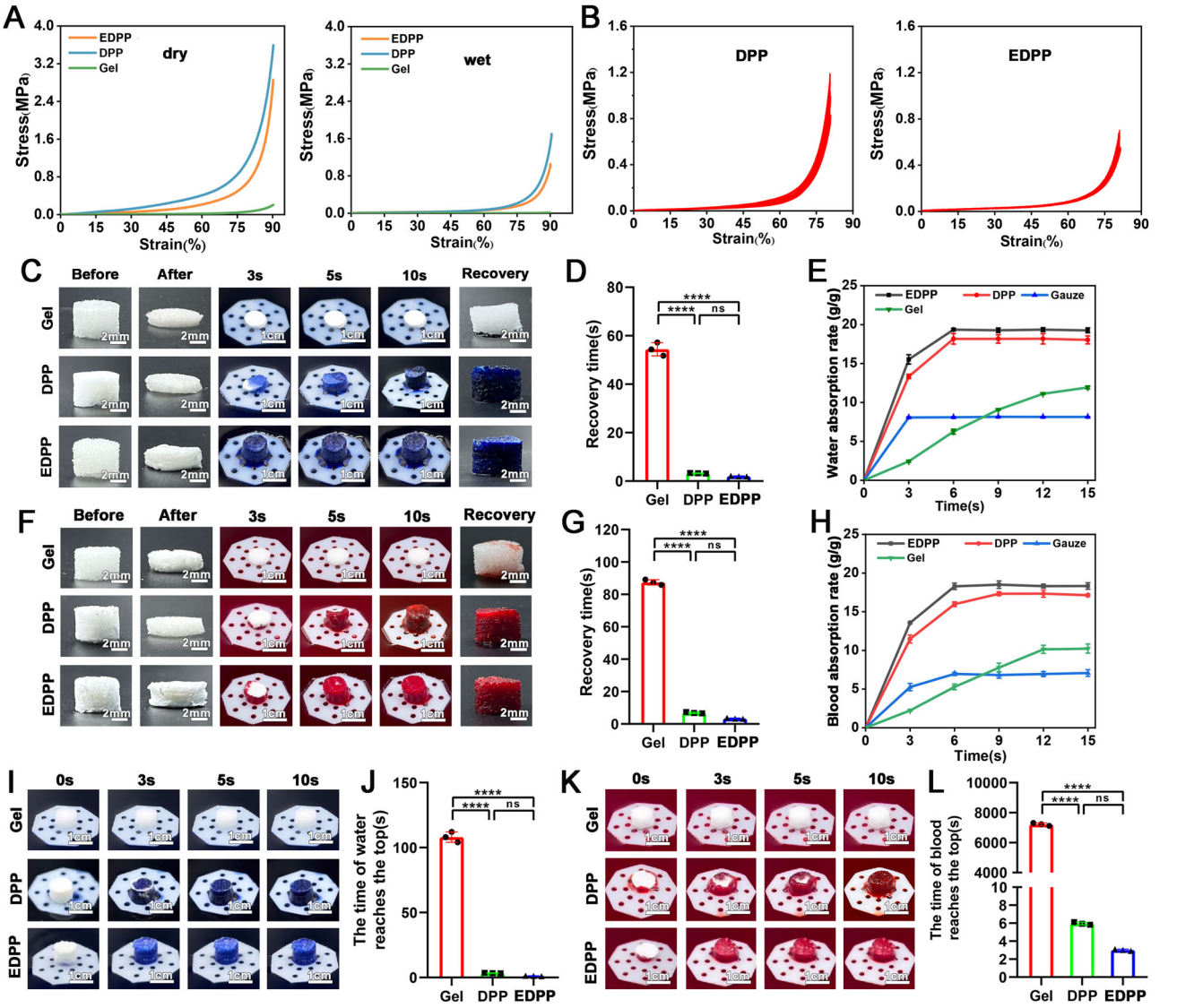

Fig. 5 | Mechanical property, shape recovery performance, and liquid absorption capacity of the expanded decellularized pomelo peel. A The compressive strain-stress curves of the DPP, EDPP, and gelatin sponge under dry and wet conditions in 90% compressive strain. **B** Cyclic compression test of the DPP and EDPP in 80% compressive strain (20 cycles). **C** Photographs of the DPP and EDPP before and after compression, and its shape recovery behaviors after absorbing water. **D** The shape recovery time of the DPP, EDPP, and gelatin sponges after absorbing water. **E** The water absorption capacity-time curves of DPP, EDPP, gelatin sponge, and gauze. **F** Photographs of the DPP and EDPP foam before and after compression, and its shape recovery behaviors after absorbing blood. **G** The shape recovery time of the DPP, EDPP, and gelatin sponges after absorbing blood. **H** The blood absorption capacity-time curves of the decellularized pomelo peel. **I** Photographs of the DPP, EDPP, and gelatin sponge siphoning water. **J** The time for water to reach the top of the DPP, EDPP, and gelatin sponge. **K** Photographs of the DPP, EDPP, and gelatin sponge siphoning blood. **L** The time for blood to reach the top of the DPP, EDPP, and gelatin sponge. $^{****}p < 0.0001$ (n = 3).

DPP was (1.013 ± 0.126) MPa and (1.723 ± 0.231) MPa, respectively, which also exceeded that of the gelatin sponge (0.014 ± 0.002) MPa (Fig. 5A and Supplementary Fig. 9). In addition, the compressive stress of EDPP was reduced compared to DPP under both dry and wet conditions (Supplementary Fig. 9). Similarly, in wet and dry conditions, DPP's tensile modulus and tensile strength were higher than EDPP's (Supplementary Fig. 10). The cyclic compression experiments revealed that the DPP and EDPP sponges could recover approximately 67.33% and 91.06% of their original height after undergoing 80% compressive strain for 20 cycles (Fig. 5B).

Following, we explored the water absorption ability and its shape recovery behaviors in water. As depicted in Fig. 5C, the photographs demonstrate the shape recovery after releasing the compression of the DPP and EDPP for 3, 5, and 10 s in water. The final recovery time for the gelatin sponge, DPP, and EDPP was (54.44 ± 2.73) s, (3.24 ± 0.14) s, and (2.01 ± 0.15) s, respectively (Fig. 5D). The DPP and EDPP reached swelling equilibrium within 6 s, significantly faster than the gelatin sponge (Fig. 5E). The maximum water absorption of gelatin sponge, DPP, EDPP, and gauze was (19.35 ± 0.16)g/g, (8.1 ± 0.069)g/g, (6.253 ± 0.316)g/g (Fig. 5E). Similarly, the compressed DPP and EDPP could revert to their original shape within 5 seconds in blood (Fig. 5F). The final recovery time for the gelatin sponge, DPP, and EDPP was (87.42 ± 1.64) s, (6.88 ± 0.4) s, and (3.37 ± 0.29);s, respectively (Fig. 5G). Additionally, EDPP and DPP were able to reach swelling equilibrium within 6 and 9 seconds, respectively, similar to the behavior observed in the gauze group (Fig. 5H). The maximum blood absorption of gelatin sponge, DPP, EDPP, and gauze was (18.95 ± 0.17)g/g, (7.96 ± 0.21)g/g, (5.95 ± 0.22)g/g in blood (Fig. 5H).

The siphon effect also affects the water and blood absorption rates of hemostatic materials. The siphoning of water and blood by the gelatin sponge, DPP, and EDPP is illustrated in Fig. 5I, K. The time required for DPP and EDPP to siphon water to the top was only 2.11 ± 0.2 s and 1.13 ± 0.185 s, respectively. And siphon blood to the top was 5.89 ± 0.5 and 3.01 ± 0.1 s (Fig. 5J, L). This is in stark contrast to the gelatin sponge, which

took significantly longer (108 ± 2.31) s in water and 7219 ± 54.88 s in blood) (Fig. 5J, L). Because of EDPP's rapid blood-absorbing ability and rapid shape recovery ability, it holds promise for expedited hemostasis in non-compressible torso hemorrhages. For intra-abdominal hemostasis applications, the compressed EDPP sponge can be loaded into a syringe, rapidly expanding from its compressed state (about 5 mm in height) to its initial state (8 mm in height) within 0.1 s after injection into water (Supplementary Fig. 11).

The hemostatic ability of EDPP in vivo

We first check the blood compatibility of EDPP because only materials with blood compatibility can be used in hemostatic applications. Supplementary Fig. 12 displays the hemolysis assay of DPP, EDPP, and gelatin sponge at various concentrations ranging from 0.625 to 2.5 mg/mL. Both DPP and EDPP, similar to the gelatin sponge, did not exhibit an obvious hemolysis phenomenon. Furthermore, quantifying the hemolysis ratio across different concentration dispersions indicated that DPP and EDPP had hemolysis ratios similar to those of the gelatin sponge (positive control). Then, we examined the hemostatic ability of EDDP in vivo.

In this study, we employed four bleeding models to validate the hemostatic efficacy of EDPP. In the rat tail-amputation model (Supplementary Fig. 13A), severe bleeding was noted in the blank, gauze, and gelatin groups following treatment with hemostatic materials. In contrast, only minimal bleeding was observed in the DPP and EDPP groups (Supplementary Fig. 13B). The total blood loss from both DPP (490.25 ± 71.36 mg) and EDPP (378.75 ± 60.31 mg) treatments was significantly lower compared to the blank (1761.25 ± 131.7 mg), gauze (1227.25 ± 97.44 mg), and gelatin (791.75 ± 143.1 mg) groups (Supplementary Fig. 13C). Furthermore, the hemostasis time for both DPP (79 ± 9.20 s) and EDPP (69 ± 5.48 s) was notably shorter than that for the blank (220 ± 9.13 s), gauze (150 ± 10.23 s), and gelatin (126.5 ± 6.03 s) groups (Supplementary Fig. 13D). In the rat liver severe cutting hemorrhage model (Supplementary Fig. 14A), the blood loss in groups treated with DPP (453.5 ± 72.41 mg) and EDPP (333 ± 42.48 mg) was significantly lower compared to the blank (1637.75 ± 85.27 mg), gauze (939.75 ± 48.31 mg), and gelatin (663 ± 73.55 mg) groups (Supplementary Fig. 14B, C). Moreover, the hemostasis time for both DPP (87.75 ± 8.46 s) and EDPP (83.75 ± 6.80 s) was notably faster than that for the blank (220 ± 9.13 s), gauze (171.5 ± 8.81 s), and gelatin (138.75 ± 5.91 s) groups (Supplementary Fig. 14D).

In the rat liver perforation model (Fig. 6A), the gauze, gelfoam, DPP, and EDPP were inserted into the liver perforated area. However, severe bleeding persisted in the gauze and gelfoam-treated groups (Fig. 6B). Conversely, the DPP (314.5 ± 9.04) mg and EDPP (169.9 ± 5.13) mg treated groups exhibited reduced blood loss compared to the blank (1249 ± 47.52) mg, gauze (865.18 ± 54.36) mg, and gelfoam (654.75 ± 44.54) mg groups (Fig. 6C). Additionally, the hemostasis time in the DPP (75 ± 6.38) s and EDPP (69.5 ± 5.07) s groups was significantly shorter than in the blank (220 ± 9.13) s, gauze (152.7 ± 8.30) s, and gelatin (124 ± 13.59) s groups (Fig. 6D). After achieving hemostasis, we left the hemostatic material in the liver defect area to further evaluate the compatibility of the hemostatic material with liver tissue (Supplementary Fig. 15). After 7 and 14 days of implantation, the DPP and EDPP were infiltrated with many cells, and more cells were infiltrated in the EDPP group. Judging from the nuclei of the infiltrating cells, there are liver cells in DPP and EDPP (Supplementary Fig. 15), indicating that DPP and EDPP are compatible with liver tissue.

In the rabbit cardiac perforation model (Fig. 6E), the blood loss in the DPP (183.03 ± 8.82 mg) and EDPP (174.1 ± 8.73 mg) groups was much less than in the blank (2648.8 ± 240.4 mg) and gauze (1127.2 ± 67.47 mg) groups, but was similar to the gelatin group (269.35 ± 8.86 mg) (Fig. 6F, G). The hemostasis time in the DPP (65.5 ± 2.89 s) and EDPP (37.5 ± 2.65 s) groups was much shorter than the blank (270.25 ± 14.06 s), gauze (218.25 ± 14.31 s), and gelatin (119 ± 13.69 s) groups (Fig. 6H). We also examined the compatibility of DPP with cardiac tissue. As shown in Supplementary Fig. 16, the treatment of EDPP is the same as that of gelfoam. There was no obvious tissue rejection reaction because of no fibrous capsule formation.

The potential hemostatic mechanism of the EDPP

Firstly, we investigated the hemoglobin binding capacity of the EDPP in vitro. Supplementary Fig. 17A illustrates the hemoglobin binding capacity of EDPP at different detection times. The blood clotting index (BCI(%)) further revealed that DPP and EDPP exhibited superior hemoglobin binding capacity compared to gelfoam and gauze (Supplementary Fig. 17B). Furthermore, the blood clotting time of DPP and EDPP was shorter than that of gauze and gelfoam, with the EDPP group exhibiting faster blood clotting than the DPP group (Supplementary Fig. 17C).

Subsequently, whole blood was co-cultured with Gelfoam, DPP, and EDPP, revealing that Gelfoam could only absorb a small amount of red blood cells and platelets (Supplementary Fig. 18A–C). In comparison, DPP and EDPP could absorb more red blood cells and platelets. Next, we co-cultured the isolated platelets with hemostatic materials to detect the activation of platelets induced by the hemostatic materials. We observed that most platelets on the surface of gelfoam remained oval shape. In contrast, a significant portion of platelets on the surface of DPP and EDPP changed their shape and exhibited activation, generating numerous pseudopods (Fig. 7A). The activation of platelets is related to the charge of the material itself. We found that gelfoam, DPP, and EDPP were negatively charged, with EDPP exhibiting the highest negative charge (−28.33 ± 0.23 mV), followed by DPP (27.3 ± 0.15 mV) and gelfoam (−24.93 ± 0.12 mV) (Fig. 7B). The negative charge carried by the hemostatic material can activate platelets, and platelet activation can be quantified by activated partial thromboplastin time (APTT), which investigates the activation of the coagulation cascade response induced by the hemostatic materials. As shown in Fig. 7C, the EDPP-treated group exhibited the shortest APTT time, which was consistent with the negative charge of the hemostatic material (Fig. 7B). Additionally, we examined the effects of EDPP on exogenous coagulation pathways and found no difference in prothrombin time (PT) among all groups (Fig. 7D). Finally, we examine the promoting effect of hemostatic materials on fibrin formation. More fibrin fibers were detected on the surface of DPP and EDPP than on the gelfoam surface (Fig. 7E).

Based on the above results, we speculate that the potential mechanism for EDPP to stop bleeding quickly is that its loose and porous structure can absorb a large number of red blood cells and platelets. Moreover, the negative charge on its surface can further activate platelets, initiating the coagulation cascade reaction and leading to rapid hemostasis, thereby promoting the formation of fibrin gel (blood clot) (Fig. 7F).

The carbonized pomelo peel (CPP) for managing infected skin wounds

A one-pot hydrothermal reaction prepared the carbonized pomelo peel (CPP) aerogel (Fig. 8A). This study discovered that CPP exhibits a photothermal effect, which could be leveraged to treat infected skin wounds (Fig. 8B). We selected three types of CPPs carbonized at different temperatures and durations. The final structure of CPP aerogels (160 °C, 8 h; 160 °C, 10 h; 180 °C, 10 h) closely resembled the original porous structure before carbonization. Initially, we assessed the photothermal efficiency of these three CPPs. We found that the temperatures of these three CPPs increased with the extension of infrared light irradiation time (Fig. 8C, D). In addition, the photothermal effect of CPP is related to the carbonization temperature and time. The photothermal effect is high when the carbonization temperature is high or the carbonization time is extended. After 10 min of irradiation, the final temperatures of the three CPPs 57.8 °C, 59.8 °C, and 61.4 °C. Following, we also explored the photothermal conversion stability of the three kinds of CPPs. After 3 cycles of irradiation, the highest temperature of the three CPPs remains the same (Fig. 8E). Suggesting all CPPs have stable photothermal conversion efficiency.

First, we tested the in vitro antibacterial effect of CPP combined with photothermal therapy. The *S. aureus* and *E. coli* were seeded on the surface of

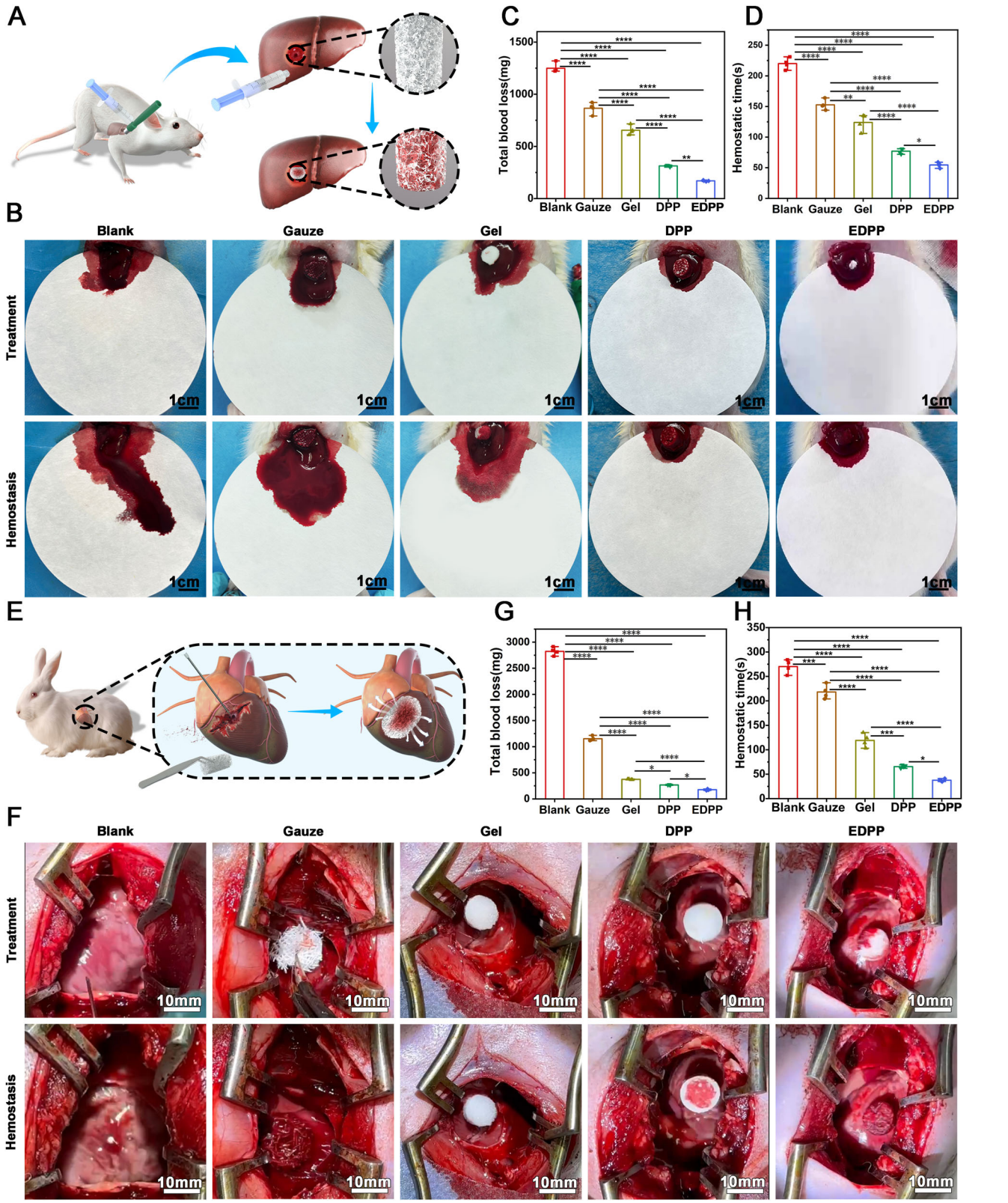

Fig. 6 | Hemostatic performance of the expanded decellularized pomelo peel (foam) on the management of rat liver-perforation and rabbit cardiac perforation hemorrhage model. A Schematic of the rat liver-perforation hemorrhage model. **B** Photographs of visual blood loss treated by DPP, EDPP, Gauze, and gelatin sponge in the rat liver-perforation hemorrhage model. The blank group was not treated with any hemostatic material. **C** The total blood loss of rats treated with DPP, EDPP, Gauze, and gelatin sponge in the rat liver-perforation hemorrhage model. **D** Hemostatic time of DPP, EDPP, Gauze, and gelatin sponge in the rat liver-perforation hemorrhage model. **E** Schematic of the rabbit cardiac perforation hemorrhage model. **F** Photographs of visual blood loss treated by DPP, EDPP, Gauze, and gelatin sponge in the rabbit cardiac perforation hemorrhage model. The blank group was not treated with any hemostatic material. **G** The total blood loss of rabbits treated with DPP, EDPP, Gauze, and gelatin sponge in the rabbit cardiac perforation hemorrhage model. **H** Hemostatic time of DPP, EDPP, Gauze, and gelatin sponge in the rabbit cardiac perforation hemorrhage model. $^{*}p < 0.05$, $^{**}p < 0.01$, $^{***}p < 0.001$, $^{****}p < 0.0001$(n = 3–4).

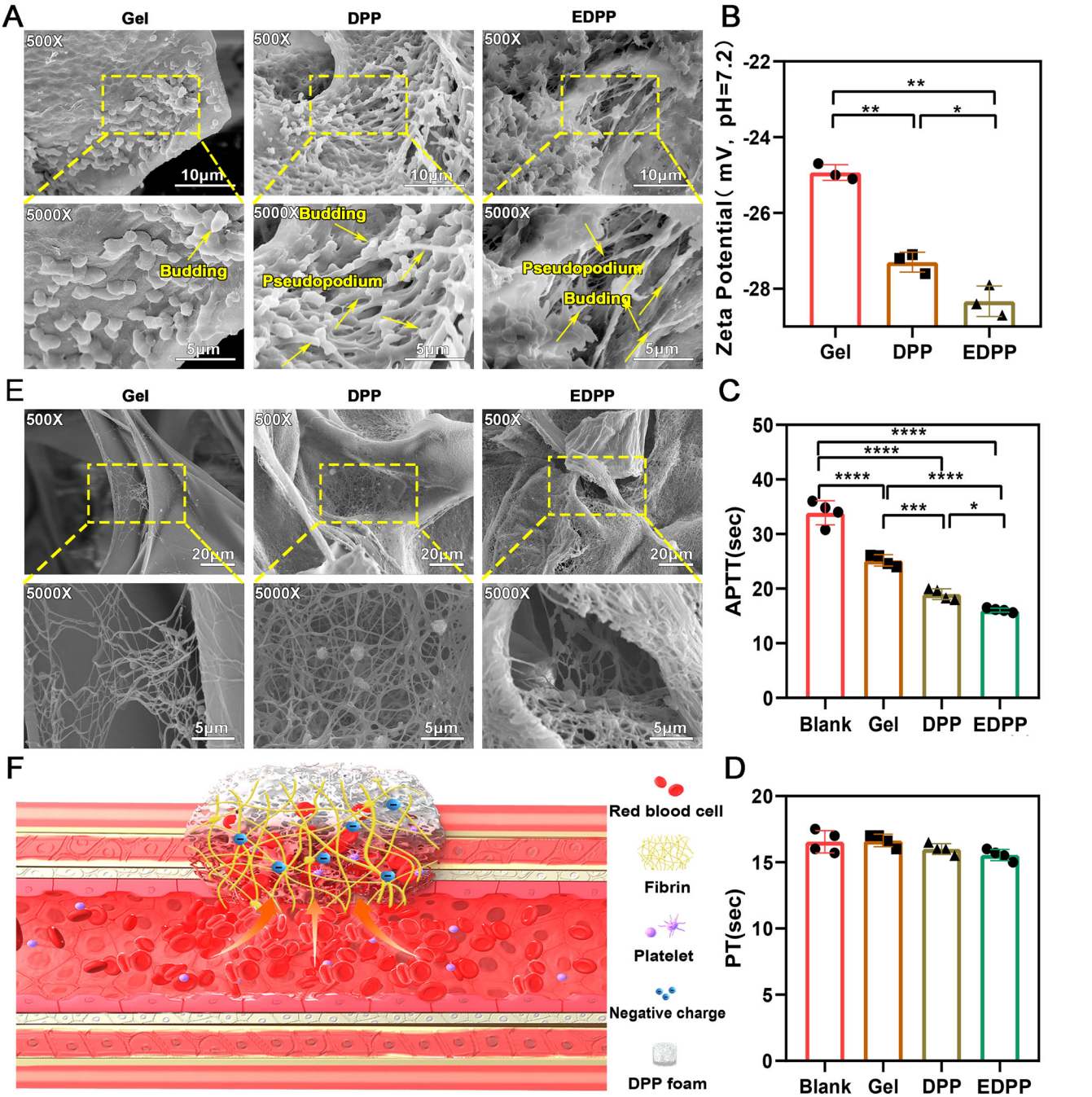

Fig. 7 | The coagulation mechanism of the expanded DPP foam. A SEM images showing the platelet activation and adhesion on the materials of DPP, EDPP, and gelatin sponge. **B** Zeta potential of DPP, EDPP, and gelatin sponge. **C**, **D** Activated partial thromboplastin time (APTT) and prothrombin time (PT) and analysis of DPP, EDPP, and gelatin sponge (n = 3). **E** SEM images showing the formation of fibrin on the materials of DPP, EDPP, and gelatin sponge. **F** Schematic diagram of the mechanism of EDPP promoting blood coagulation. *$p < 0.05$, **$p < 0.01$, ***$p < 0.001$, ****$p < 0.0001$ (n = 3–4).

different CPPs, and then treated with infrared-irradiation for 10 min. We found that *S. aureus* (Supplementary Fig. 19) and *E. coli* (Supplementary Fig. 20), when treated with infrared irradiation, collapsed and died. Further quantitative analysis found that the antibacterial rates of CPP (160 °C, 8 h), CPP (160 °C, 10 h), and CPP (180 °C, 10 h) combined with photothermal therapy against *S. aureus* were 92%, 97%, and 94%, respectively (Supplementary Fig. 21). And the antibacterial rates of CPP (160 °C, 8 h), CPP (160 °C, 10 h), and CPP (180 °C, 10 h) combined with photothermal therapy against *E. coli* were 94%, 98%, and 96%, respectively (Supplementary Fig. 22). In a biofilm-infected skin wound model, we tested the in vivo antibacterial effect of CPPs combined with photothermal therapy and its ability to promote infectious wound healing. After the biofilm-infected wound model was established, CPP dressing combined with photothermal therapy was given (Supplementary Fig. 23A). After 3 days of treatment, the remaining bacteria in the wound were detected, revealing only trace amounts of bacteria remaining in the three photothermal therapy groups (Supplementary Fig. 23B). The in vivo antibacterial rates of *S. aureus* by combined photothermal treatments with CPP (160 °C, 8 h), CPP (160 °C, 10 h), and CPP (180 °C, 10 h) was 98%, 99%, and 99%, respectively (Supplementary Fig. 23C). Giemsa staining of the wound tissue further illustrated that in the CPPs group without photothermal treatment, a substantial presence of bacteria persisted in the wound tissue at both 3 and 7 days post-surgery. In contrast, in the CPPs group treated with photothermal therapy, only a few bacteria were observed in the wound tissue after 3 days of treatment. By the

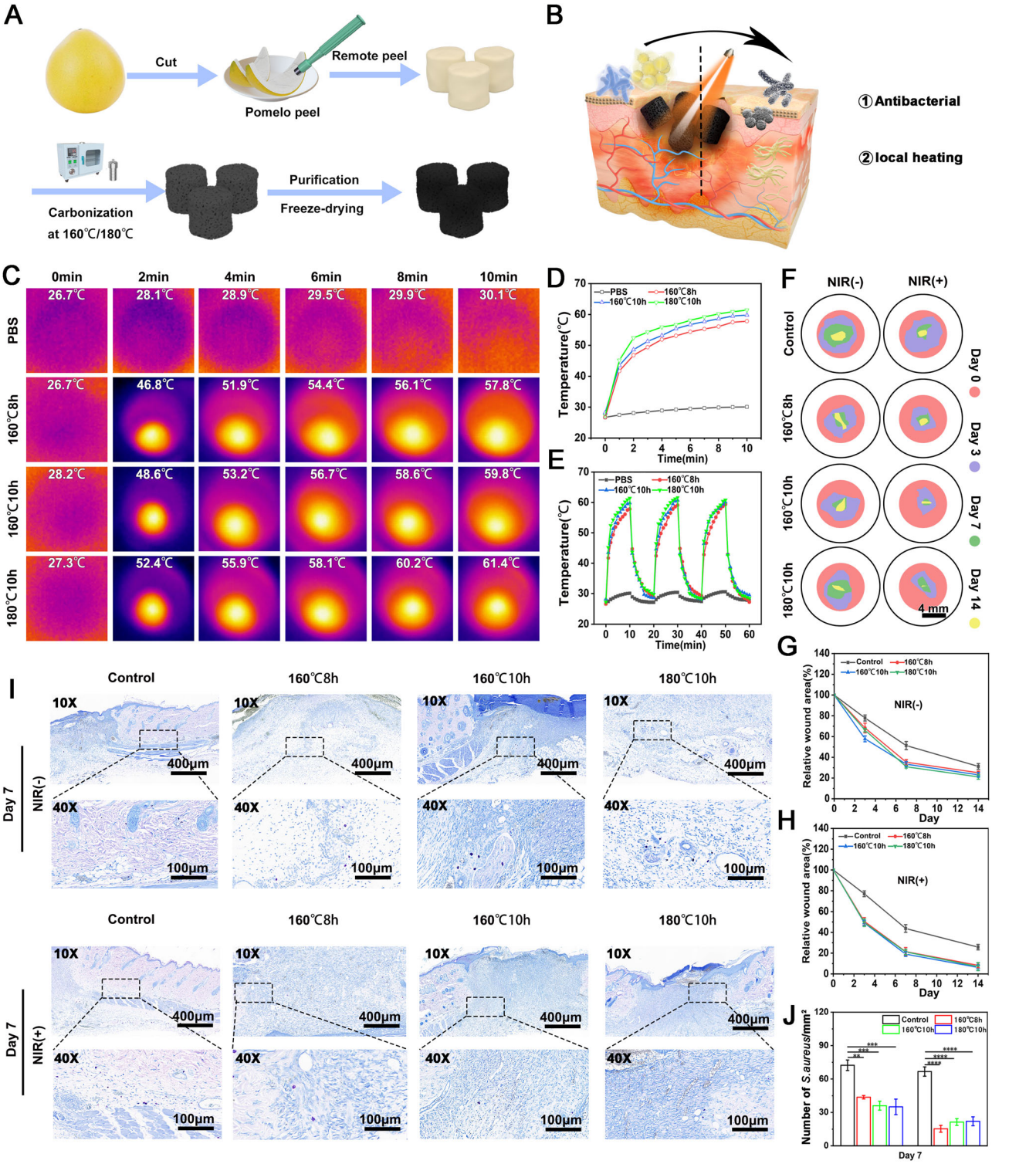

Fig. 8 | The carbonized pomelo peel (CPP) effectively eradicates bacterial biofilms and accelerates wound healing. **A** The schematic diagram shows the preparation processes of CPP. **B** The application of CPP on the infected wound healing. **C** Infrared photothermal images of different CPPs after near-infrared irradiation for 0 min, 2 min, 4 min, 6 min, 8 min, and 10 min, respectively. **D** Temperature quantification of different CPPs with the treatment of near-infrared irradiation for different times. **E** Temperature changes of different CPPs with repeated near-infrared irradiation. **F–H** The residual wound size of the wound treated with different CPPs in combination with NIR on day 3, 7, and 14. **I** The Giemsa staining of skin wounds treated with different CPPs in combination with NIR treatment for 7 days. **J** The residual *S. aureus* within wound tissues after the treatment of CPPs in combination with NIR treatment for 7 days. $^{**}p < 0.01$, $^{***}p < 0.001$, $^{****}p < 0.0001$ (n = 3).

7th day post-surgery, no bacteria were detected in the wound tissue with photothermal therapy (Fig. 8I, J and Supplementary Fig. 24).

In addition, the wound healing rate of the photothermal treatment group was significantly faster than that of the group without photothermal treatment (Fig. 8F–H and Supplementary Fig. 25). The histological observations revealed that the wounds treated with different CPPs in combination with NIR had significant granulation formation compared to the control group after 3 days of treatment. In addition, the epidermal tongue at

the edge of the wound of all CPP groups with photothermal treatment had already stuck out (Supplementary Fig. 26). After 7 days of treatment, photothermal-treated wounds had significant granulation tissue formation and re-epithelialization. The epithelialization rate of wounds without photothermal treatment was significantly lower than that of the photothermal treatment group (Supplementary Fig. 26). After 14 days of treatment, although all wounds had been closed, there was obvious hair follicle regeneration in the middle of the wound in the photothermal treatment group (Supplementary Fig. 26).

Discussion

This project originated from an accidental discovery in everyday life. After being placed in water, the air-dried pomelo peels could quickly revert to their original shape. Interestingly, washing hands with these pomelo peels left the skin feeling smooth, similar to applying a facial mask. This experience inspired me to research pomelo peel material. We first investigated the compounds contained in pomelo peel through a literature review. It has been reported that pomelo peel not only contains essential vitamins and minerals, but also many bioactive molecules, such as phenolic, coumarin, flavonoid, and limonoid constituents[11–13]. These compounds are often used in anti-inflammatory and antioxidant treatments[14,15]. One of the reasons why chronic wounds, such as diabetic foot ulcers, are difficult to heal is due to the persistent chronic inflammatory response and the presence of large amounts of reactive oxygen species. Therefore, we decellularized pomelo peel and expanded it to enhance its porosity and make it softer, which will suit skin wound healing. The in vivo results confirmed that pomelo peel could promote diabetic wound healing, demonstrating an effect equivalent to that of the collagen sponge in the positive control group (PELNAC). However, unlike the collagen sponge group, which exhibited a mild immune response, the inflammatory reaction in wounds treated with pomelo peel was stronger, yet still conducive to the pro-regenerative type. We speculate that the polyphenols, flavonoids, and other chemicals in pomelo peel regulate the wound's inflammatory response. This regulation transforms the immune responses from chronic to acute inflammatory responses, allowing the wound to enter the normal healing process.

Then, we observed the internal structure of the pomelo peel. We found that its internal structure is an interpenetrating pore structure similar to a commercial gelatin sponge, which plays a critical role in water/blood absorption[16,17]. The interpenetrating pore structure creates a larger surface area than non-porous or less porous materials. This increased surface area allows more contact points with water or blood, significantly improving absorption efficiency[18]. In addition, the interconnected network of pores facilitates capillary action, which helps draw water or blood into the material. Meanwhile, it could prevent saturation at a single point and enhance overall absorption capacity[19,20]. In the presented study, the expanded pomelo peel demonstrates the ability to quickly absorb blood and water owing to the increased porosity and interpenetrating pore structure.

Photothermal therapy has emerged as a promising technique for wound repair, leveraging materials that convert light into heat to promote healing and eliminate infections[21,22]. This approach is particularly effective against multidrug-resistant bacteria and in enhancing tissue regeneration. The existing photothermal materials are mainly divided into plasmonic metal nanostructures, semiconductors, carbon-based, and polymer-based materials[23]. Although photothermal materials offer significant potential for improving wound healing and combating infections, addressing their biocompatibility, stability, and controlled release mechanisms is crucial for their successful translation into clinical practice. Many photothermal materials, especially those involving metal nanoparticles[24] or graphene derivatives[25], pose potential risks of cytotoxicity. Ensuring these materials are biocompatible and safe for long-term use is a critical challenge. Besides, maintaining the stability of photothermal agents within the scaffold under physiological conditions is essential. For example, the hydrogel may face degradation or mechanical failure, reducing its effectiveness in wound healing. Finally, producing these advanced photothermal materials on a large scale can be costly and technically challenging, limiting their widespread clinical application. In contrast, the photothermal material based on carbonized pomelo peel that we developed features a simple preparation method and stable photothermal efficiency, eliminating the need for a carrier material. Additionally, it is free from potentially cytotoxic components such as graphene and nanometal oxides, making it a safer alternative.

Conclusion

In summary, using two environmentally friendly manufacturing techniques, we have successfully transformed pomelo peel into biomedical devices for rapid hemostasis and wound management. For one thing, the pomelo peel was decellularized and then subjected to a modified gas-foaming process to expand the decellularized pomelo peel, enhancing its porosity. In wound healing experiments, the expanded pomelo peel significantly promoted granulation tissue formation, collagen deposition, and wound closure compared to positive control groups. For rapid hemostasis, expanded pomelo peel demonstrated quick liquid absorption and shape recovery post-compression, efficiently activating platelets to achieve rapid coagulation. For another, the pomelo peel was carbonized to create a carbon-based material with photothermal properties. When applied to infected skin wounds, the photothermal effect effectively eradicated bacterial biofilms, thereby accelerating wound healing. Additionally, the widespread availability of pomelo peel and purely physical processing methods, such as modified gas-foaming and carbonization technologies, enable large-scale production without generating waste.

Our research has validated the feasibility of our approach. In future studies, we will focus on utilizing "black" photothermal materials derived from pomelo peels to manage various chronic wounds. Chronic wound treatment and care comprise approximately 5% of our nation's medical insurance expenditures. Firstly, the pomelo peel photothermal material we developed can effectively clear bacterial infections in chronic wounds and prevent the emergence of drug-resistant bacteria. Secondly, carbonized pomelo peel is a porous carbon-based material that can efficiently absorb wound exudate and deodorize, thereby enhancing the patient's quality of life and social interactions. Finally, the tissue temperature around chronic wounds tends to be low. The photothermal effect of the grapefruit peel material can increase the local wound temperature, promote tissue metabolism, and accelerate healing. However, this work also has shortcomings, such as the lack of functional validation of the identified signaling pathways. We will continue to explore its pro-healing mechanism in future work. Overall, this study underscores the potential of repurposing agricultural waste into high-value biomedical materials, contributing to sustainable resource utilization and advanced healthcare solutions.

Methods

Preparation of decellularized pomelo peel sponge

First, we removed the Shatian pomelo pulp and used a blade to cut off the thickest part of the pomelo peel to expose the white, soft inner layer. The peel was then cut into 5 mm thick discs and washed thrice with ultrapure water. These discs were subsequently soaked in a 10% w/v SDS solution on a low-speed shaker at room temperature for 5 days. After this period, the samples were washed three times with ultrapure water and immersed in a solution containing 0.1% Triton-X100 (v/v) and 10% sodium hypochlorite (v/v) for 2 days. The samples were soaked in Tris-HCL (pH 8.5) for 2 days. Finally, the samples were sterilized by soaking them in alcohol for 2 h, followed by three washes with sterile PBS and freeze-drying. The freeze-dried samples were further sterilized using UV light for 30 min and stored aseptically.

Preparation of expanded decellularized pomelo peel sponge

Place approximately 1 g of dry ice and a piece of decellularized pomelo peel sponge into a 30 ml Oak Ridge centrifuge tube. Once the dry ice transitions into liquid carbon dioxide, loosen the lid and remove the expanded decellularized pomelo peel sponge from the tube. At atmospheric pressure, the cap is unscrewed and the liquid carbon dioxide sublimates into gaseous carbon dioxide. The sponge is immersed in the liquid carbon dioxide and

the gas flows under the surface, causing the sponge to expand. The whole process is carried out at atmospheric pressure and room temperature, and the duration time is within 1 s. At room temperature (25 °C), the liquid carbon dioxide vaporizes violently and the pressure in the closed system (tube) rises rapidly to 64 atm (about 6.5 MPa), and we loosened the lid during the experiment to avoid exceeding the pressure limit of the container. Sterilize the samples using UV light for 30 min and store them aseptically.

Preparation of carbonized pomelo peel aerogel

The carbonized pomelo peel was synthesized using a hydrothermal method. First, the outer skin of the Shatian pomelo peel was removed, and the peel was cut into appropriately sized pieces. These pieces were then placed into a stainless steel autoclave with a polytetrafluoroethylene (PTFE) liner (LC-KH-5, Lichen). The material was loaded into the reaction autoclave. The following precautions should be taken when using the reaction autoclave: The loading volume should be less than 70% of the capacity. Tighten the bolts of the autoclave and place the autoclave in the oven for high-temperature reaction. Open the autoclave only after it has cooled down naturally to room temperature. Do not open at high temperature and pressure, it may cause explosion. The ovens were preheated to 160 °C and 180 °C, respectively. The autoclave was put into the preheated oven at 160 °C for 8 h, 10 h, and 180 °C for 10 h, respectively. After the reaction, the autoclave was allowed to cool to room temperature. The product was then removed and sequentially immersed in anhydrous ethanol and deionized water, followed by freeze-drying at −20 °C for 24 h.

In vivo hemostatic ability

The Ethical Committee of the Second Affiliated Hospital of Nanchang University approved all animal procedures. The animals used in the experiments were purchased from Tianqin Biotechnology Company and housed in a specific pathogen-free laboratory animal facility at Nanchang University (Nanchang, China). The animal ethical inspection number is NCULAE 20220928014. The decellularized pomelo peel scaffold was prepared with a diameter of 6 mm and a height of 5 mm.

Rat liver perforation model. After the male rats were anesthetized, the liver was exposed through an abdominal incision. The liver was lifted and placed on pre-weighed filter paper. A circular perforation wound was then created on the liver to induce bleeding. The decellularized pomelo peel scaffold was compressed and inserted into the wound cavity. Gelatin sponge and gauze were the control group, while the untreated wound was the negative control. The entire hemostasis process was recorded with a digital camera. The total weight of blood absorbed by the filter paper and the hemostatic agent was measured, and the hemostasis time was recorded with a timer. Samples were collected for subsequent histological analysis.

Rat tail amputation model. After anesthetizing the male rats, a pre-weighed filter paper was placed under the tail, which was then amputated 4 cm from the tip. The decellularized pomelo peel scaffold was immediately applied to the bleeding site. Gelatin sponge and gauze were the control group, while an untreated wound was the negative control. The entire hemostasis process was recorded with a digital camera. The total weight of blood absorbed by the filter paper and the hemostatic agent was measured, and the hemostasis time was recorded using a timer.

Rat liver resection model. After the male rats were anesthetized, the liver was exposed through an abdominal incision. The liver was then lifted and placed on the pre-weighed filter paper. Next, a quarter of the liver was excised, and the wound was immediately filled with the compressed decellularized pomelo peel scaffold. Gelatin sponge and gauze were used as the control group, while an untreated wound was the negative control. The entire hemostasis process was recorded with a digital camera. The total weight of blood absorbed by the filter paper and the hemostatic agent was measured, and the hemostasis time was recorded using a timer.

Rabbit cardiac perforation homeostasis. After the male rabbits were anesthetized, the chest was opened along the midline of the sternum to expose the heart. A hole was then created in the anterior wall of the right ventricle using a 22-gauge syringe needle, and the wound was immediately filled with a compressed decellularized pomelo peel scaffold. Gelatin sponge and gauze served as the control group, while an untreated wound was used as the negative control. The entire hemostasis process was recorded with a digital camera. The total weight of blood absorbed by the filter paper and the hemostatic agent was measured, and the hemostasis time was recorded using a timer. Samples were also collected for further histological analysis.

Wound healing

All animal procedures were approved by the Ethical Committee of the Wenzhou Institute, University of Chinese Academy of Sciences. The animals used in these experiments were purchased from the Animal Center of Zhejiang Province and maintained in the specific pathogen-free laboratory animal facility of the Wenzhou Research Institute. The animal ethics approval number is WIUCAS23101201. The decellularized pomelo peel scaffold was prepared with a diameter of 8 mm and a height of 1 mm.

Male ICR mice were injected intraperitoneally with streptozotocin (50 mg/kg, dissolved in 50 mM sodium citrate buffer, pH 4.5, prepared immediately before use) at one-day intervals five times to model the whole skin defect. 2% isoflurane/1% oxytetracycline was used to anesthetize the mice. A 4×4 cm^2 area of the back of the mouse was shaved, and then the exposed skin was wiped with povidone-iodine solution. A perforator was used to create an 8-mm-diameter wound on each side of the back, with a distance of 1.5–2 cm between the two wounds, and the wounds were secured with silicone fixation rings. The wound without any treatment was the control group, the PELNAC and Lando-treated wounds were set as the positive group, and the DPP and EDPP-treated wounds were the experimental group. Samples were collected at 3 days, 7 days, 14 days, and 21 days, respectively, and the wound closure rate was measured by Image J, and the samples were also followed by further histological analysis. The samples collected on day 7 were sent for RNA-seq analysis. The wound without any treatment was the control group, the PELNAC and Lando-treated wounds were set as the positive group, and the DPP and EDPP-treated wounds were the experimental group. Samples were collected at 3 days, 7 days, 14 days, and 21 days, respectively, and the wound closure rate was measured by Image J, and the samples were also followed by further histological analysis. The samples collected on day 7 were sent for RNA-seq analysis. The calculation of wound closure rate: Wound closure rate (%) = $(Si - St)/Si \times 100\%$. Si represented the initial wound area, and St represented the wound area at 3, 7, 14, and 21 days. The calculation of re-epithelialization rate: (The distance of re-epithelialization/total width of the initial wound) × 100%.

In vivo antimicrobial experiments

The ethical committee of the Second Affiliated Hospital of Nanchang University approved all procedures involving animals. All animals used in the experiments were purchased from Tianqin Biotechnology Company and were housed in the specific pathogen-free laboratory animal facility at Nanchang University (Nanchang, China). The animal ethics approval number is NCULAE 20221031135.

Firstly, the male rats were randomly divided into 8 groups, 3 rats in each group. The rats were anesthetized with 2% isoflurane and fixed on the operating table. A wound with an 8 mm diameter was created on the back of the rats using a skin perforator. 100ul of *Staphylococcus aureus* bacterial solution was applied to the surface of the wound for 24 h to create a model of the infected wound, different groups of carbonized pomelo peel were placed on the wound, and the wound was irradiated with an infrared laser for 10 min on days 1 and 3. Rats without light treatment were used as a control group. The wound area of rats was measured on days 3, 7, and 14, and skin tissues from the wound area were collected and fixed with 4% paraformaldehyde for histological analysis, such as H&E staining, Giemsa staining, and Masson staining. Pus solution was dipped from the wound on

day 3 and placed in 3 ml of PBS solution for plate application. Subsequently, the bacterial solution was diluted to 10^{-3}, spread evenly on the agar medium, and incubated at 37 °C for 12 h. The number of colonies on the agar medium was counted. The formula for calculating the antimicrobial rate of the carbonized pomelo peel was as follows:

$$\text{Antimicrobial rate}(\%) = (A_2 - A_1)/A_2 \times 100\%$$

A_2 is the number of colonies in the wound without treatment, and A_1 is the number of colonies in the wound after being treated with the sample.

Statistical analysis

All results were expressed as mean ± standard deviation ($n \geq 3$). Statistical comparisons among multiple groups were performed using one-way analysis of variance. Statistical significance was considered at $^{*}p < 0.05$, $^{**}p < 0.01$, $^{***}p < 0.001$ and $^{****}p < 0.0001$.

Data availability

Data and materials are reported in the study are available from the corresponding authors (chensx@ucas.ac.cn (S. Chen)) upon reasonable request.

Received: 30 January 2025; Accepted: 22 September 2025;
Published online: 12 November 2025

References

1. Wegst, U. G. K., Bai, H., Saiz, E., Tomsia, A. P. & Ritchie, R. O. Bioinspired structural materials. *Nat. Mater.* **14**, 23–36 (2015).
2. Wang, Y. et al. Nature-inspired micropatterns. *Nat. Rev. Methods Prim.* **3**, 68 (2023).
3. Tang, T.-C. et al. Materials design by synthetic biology. *Nat. Rev. Mater.* **6**, 332–350 (2021).
4. Li, T. et al. Developing fibrillated cellulose as a sustainable technological material. *Nature* **590**, 47–56 (2021).
5. Vesth, T. C. et al. Investigation of inter- and intraspecies variation through genome sequencing of Aspergillus section Nigri. *Nat. Genet.* **50**, 1688–1695 (2018).
6. Xiao, L., Ye, F., Zhou, Y. & Zhao, G. Utilization of pomelo peels to manufacture value-added products: a review. *Food Chem.* **351**, 129247 (2021).
7. Tocmo, R., Pena-Fronteras, J., Calumba, K. F., Mendoza, M. & Johnson, J. J. Valorization of pomelo (Citrus grandis Osbeck) peel: a review of current utilization, phytochemistry, bioactivities, and mechanisms of action. *Compr. Rev. Food Sci. Food Saf.* **19**, 1969–2012 (2020).
8. Jiang, J. et al. CO2-expanded nanofiber scaffolds maintain activity of encapsulated bioactive materials and promote cellular infiltration and positive host response. *Acta Biomater.* **68**, 237–248 (2018).
9. Yang, G. et al. Super-elastic carbonized mushroom aerogel for management of uncontrolled hemorrhage. *Adv. Sci.* **10**, 2207347 (2023).
10. Yang, G. et al. Magnesium/gallic acid bioMOFs laden carbonized mushroom aerogel effectively heals biofilm-infected skin wounds. *Biomaterials* **302**, 122347 (2023).
11. Su, B. et al. Qualitative and quantitative analyses of the chemical components of peels from different pomelo cultivars (Citrus grandis [L.] Osbeck) based on gas chromatography–mass spectrometry, ultraperformance liquid chromatography-q-exactive orbitrap-MS, and high-performance liquid chromatography-photodiode array detection. *ACS Omega* **8**, 6253–6267 (2023).
12. Van Hung, P., Yen Nhi, N. H., Ting, L. Y. & Lan Phi, N. T. Chemical composition and biological activities of extracts from pomelo peel by-products under enzyme and ultrasound-assisted extractions. *J. Chem.* **2020**, 1043251 (2020).
13. Wandee, Y., Uttapap, D. & Mischnick, P. Yield and structural composition of pomelo peel pectins extracted under acidic and alkaline conditions. *Food Hydrocoll.* **87**, 237–244 (2019).
14. Zhao, Y.-L. et al. Anti-inflammatory effect of pomelo peel and its bioactive coumarins. *J. Agric. Food Chem.* **67**, 8810–8818 (2019).
15. Abd Rahman, N. F., Shamsudin, R., Ismail, A., Shah, N. N. A. K. & Varith, J. Effects of drying methods on total phenolic contents and antioxidant capacity of the pomelo (Citrus grandis (L.) Osbeck) peels. *Innov. Food Sci. Emerg. Technol.* **50**, 217–225 (2018).
16. Guo, B., Dong, R., Liang, Y. & Li, M. Haemostatic materials for wound healing applications. *Nat. Rev. Chem.* **5**, 773–791 (2021).
17. Dong, R., Zhang, H. & Guo, B. Emerging hemostatic materials for non-compressible hemorrhage control. *Natl. Sci. Rev.* **9**, nwac162 (2022).
18. Li, X.-F. et al. Emerging materials for hemostasis. *Coord. Chem. Rev.* **475**, 214823 (2023).
19. Yu, P. & Zhong, W. Hemostatic materials in wound care. *Burns Trauma* **9**, tkab019 (2021).
20. Lu, X., Li, X., Yu, J. & Ding, B. Nanofibrous hemostatic materials: structural design, fabrication methods, and hemostatic mechanisms. *Acta Biomater.* **154**, 49–62 (2022).
21. Cui, X. et al. Photothermal nanomaterials: a powerful light-to-heat converter. *Chem. Rev.* **123**, 6891–6952 (2023).
22. Zhi, D., Yang, T., O'Hagan, J., Zhang, S. & Donnelly, R. F. Photothermal therapy. *J. Control. Release* **325**, 52–71 (2020).
23. Zhang, J., Chen, H., Duan, X., Sun, H. & Wang, S. Photothermal catalysis: from fundamentals to practical applications. *Mater. Today* **68**, 234–253 (2023).
24. Makvandi, P. et al. Metal-based nanomaterials in biomedical applications: antimicrobial activity and cytotoxicity aspects. *Adv. Funct. Mater.* **30**, 1910021 (2020).
25. Xiao, Y. et al. Synthesis and functionalization of graphene materials for biomedical applications: recent advances, challenges, and perspectives. *Adv. Sci.* **10**, 2205292 (2023).

Acknowledgements

This work was financially supported by the National Natural Science Foundation of China (grant no. 82472551 to S.C., grant no. 82360446 to W.W.); the Zhejiang Provincial Natural Science Foundation of China (grant no. LR24H150001 to S.C.); the Wenzhou Science and Technology Major Project (grant nos. ZY2022026, ZY2023005 to S.C.).

Author contributions

W.W., J.Y., Z.H., and Y.F. performed experiments and analyzed the results. Z.W. analyzed the data. S.C. planned the experiments and wrote the whole manuscript.

Competing interests

The authors declare no competing interests.

Additional information

Supplementary information The online version contains supplementary material available at https://doi.org/10.1038/s43246-025-00969-y.

Correspondence and requests for materials should be addressed to Zhengquan Wang or Shixuan Chen.

Peer review information *Communications Materials* thanks Yanhuai Ding, Suryasarathi Bose and the other anonymous reviewers for their contribution to the peer review of this work. A peer review file is available.